Multi-Arm Post-Docking Spacecraft Dynamics Using Penalty Methods

Andrew Morell[*], João Vaz Carneiro[*], Leah Kiner[*], and Hanspeter Schaub[†]

University of Colorado, Boulder, CO, 80309

As concepts for physical spacecraft docking emerge to manage space debris and service operational satellites, there is a growing need for implementable simulation software tools modeling the resulting complex multi-body dynamics. To avoid the complexities arising from analytically solving for single spacecraft models representing the post-docking spacecraft dynamics, this work focuses on coupling the individual dynamics of the docked spacecraft through holonomic constraints enforced by numerical penalty methods. Expanding upon prior work, several constraints are derived and implemented in a software simulation including a 2-degree-of-freedom (DOF) sliding arm constraint and a 2-DOF rotating arm constraint. A multi-arm rigid 6-DOF constraint is then developed that fully couples the relative dynamics between the spacecraft using three of either 2-DOF constraint arms. Individual 2-DOF constraint arms are first validated by analyzing that the appropriate degrees-of-freedom are released. The multi-arm rigid constraint is then validated by showing all degrees-of-freedom are constrained and that constraint violations are sufficiently small in magnitude compared to spacecraft size. Finally the rigid constraint is tested with orbital and attitude maneuvers applied to the chaser spacecraft to verify that constraint violations remain sufficiently small when stressed with excited spacecraft motion.

I. Introduction

With the ever-increasing density of objects in space, the sustainability of Earth's most desired orbits has become a focus of both commercial and government space agencies. Whether the intention is to remove defunct satellites from orbit or service operational satellites running out of fuel, physical spacecraft docking has become the dominantly proposed architecture for doing so. Enabling technologies to in-space servicing, assembly, and manufacturing (ISAM) has experienced significant advancements over the past decade. A review by Dr. Bryan L. Benedict of Intelsat from 2013 outlines servicing missions both completed and proposed including Northrop Grumman's Mission Extension Vehicle as an active provider of life extension technology to Intelsat [1]. Around the same time in 2020 the Institute for Defense Analyses (IDA) conducted an extensive assessment of global trends in ISAM finding over 100 entities internationally actively engaged in ISAM activities [2]. Although the IDA identifies guidance, navigation, and controls as critical or desirable for all ISAM activities, it focuses on the rendezvous and proximity operations (RPO) aspect leaving out attention to post-docked dynamics. Post-docking dynamics requires its own extensive simulation analysis to ensure a successful mission design, and is the focus of this paper.

Simulating the post-docked joint dynamics of a resulting two spacecraft system is often performed using a surrogate single spacecraft model. This requires deriving new equations of motion tracking the translation and rotation of a joint center of mass with all the same components of each individual spacecraft. Analytically solving for the post-docking dynamics of each spacecraft is a complex and lengthy process requiring precise knowledge of each spacecraft's components, making it a mission-specific process. The resulting dynamics is far from trivial as each spacecraft can have active attitude control devices, articulated hinged solar panels or antennas, thrusters, and more resulting in a large state space. In such a single spacecraft model assuming a rigid docking arm, the structural forces and torques from the docking arm disappear. Alternatively, these otherwise internal forces can be applied as external forces to each individual spacecraft model to simulate the same resulting motion using the already existing individual equations of motion. However, the exact internal force is just as complex to analytically solve for as a single spacecraft model. Instead numerical penalty methods can be used to approximate a constraint force that corrects any constraint violations.

---

*Graduate Research Assistant, Ann and H.J. Smead Department of Aerospace Engineering Science, University of Colorado, Boulder, 431 UCB, Colorado Center for Astrodynamics Research, Boulder, CO, 80309. AIAA Student Member

†Professor and Department Chair, Schaden Leadership Chair, Ann and H.J. Smead Department of Aerospace Engineering Sciences, University of Colorado, Boulder, 431 UCB, Colorado Center for Astrodynamics Research, Boulder, CO, 80309. AAS Fellow, AIAA Fellow.

Vaz Carneiro et al. take this approach by applying constraint forces approximated using the Baumgarte Stabilization Method (BSM) [3] to couple the dynamics of two spacecraft docked in orbit through a single arm and implement it in several scenarios [4,5]. Vaz Carneiro et al. validate this constrained dynamics approach in [4] with simplified spacecraft in Matlab simulations. Vaz Carneiro et al. then validate with complex models in [5] using the Basilisk Simulation Framework*[6]. Basilisk's modular architecture enabled complexity through the addition of its models for reaction wheels [7], flexing solar panels [8], and a sloshing fuel tank [9]. The results showed that the existing dynamical models of two different spacecraft can be coupled through constraints to create a system that accurately replicates the joint dynamics as if the equations of motion had been re-derived as a single spacecraft after docking.

Whereas Northrop Grumman's MEV [10] and NASA's proposed OSAM-1 [11] missions use a single arm to dock, ESA's ClearSpace-1 [12] and Astroscale's LEXI [13] planned servicing architectures includes four connection points. Multiple docking arms distributed and controlled symmetrically with respect to an axis coincident with the servicing spacecraft's center of mass helps reduce reactionary translation of the spacecraft hub when attempting to dock with a chaser spacecraft. Therefore, the concept of enforcing multi-arm spacecraft coupling is of interest as an extension to previous work. Concept renders of multi-arm architectures are shown in Fig. 1.

(a) Astroscale's LEXI model [13].   (b) ESA's ClearSpace-1 model [12].
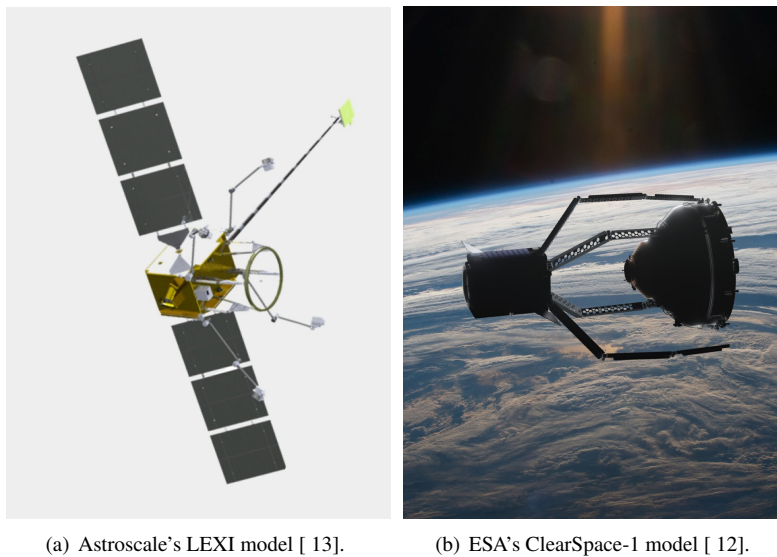
Fig. 1   Model renders of single vs. multi-arm constraint architectures.

Motivated by this alternative multi-arm architecture, this work explores applying multiple holonomic constraints to simulate multi-arm coupling between two spacecraft. Gasbarri and Pisculli investigate post-docked maneuver control using a two-arm architecture and apply holonomic constraints to enforce point compatibility between arm end effectors and their respective connection points on the target vehicle restricting all degrees of freedom at each point [14]. Stolfi et al. use a similar two-arm architecture with holonomic constraints enforcing point compliance between the robotic arm end effectors and target vehicle connection points [15]. Gasbarri and Pisculli explicitly state the use of the BSM to approximate constraint forces and torques whereas Stolfi et al. simply state the use of a Lagrange multiplier to scale their constraint force. This work varies from both Gasbarri and Pisculli and Stolfi et al. by defining holonomic constraints as a relationship between the base of the connecting arm on the chaser spacecraft and the connection point corresponding to the end of the connecting arm on the target vehicle. Therefore, the constraint in this work defines an attribute of the connecting arm whereas previous work considers only point coincident constraints. This allows specific degrees-of-freedom (DOF) to be released in the constraint formulation emulating either a 1-DOF telescoping or pivoting connection arm. In a nominal docking scenario the resulting fully constrained system would ideally no longer expose the released DOF. Although in a capture phase of a mission during which some arms attach before others then the resulting motion as well as knowledge of the constraint force applied by each arm are desired.

Vaz Carneiro et al. prove the single arm concept of the holonomic constraint in [5] by observing the resulting constraint violations when enforcing several different constraint options including a length only constraint, a length

---

constraint with one end completely rotationally fixed to a spacecraft, and a length constraint with both spacecraft connection points completely rotationally fixed. In this work, two new constraint options are developed: a sliding arm and a rotating arm. With a focus on the performance of controllers applied to the joint spacecraft system, neither Gasbarri and Pisculli or Stolfi et al. show the resulting constraint violations using their constraint formulations whereas the constraint performance is the primary concern of this work.

Section II defines the dual spacecraft system with multiple connecting arms followed by Section III which formulates the constraints forces and torques applied to each spacecraft enforcing the connections between them. In Section IV the individual arm constraint formulations are validated before combinations of three constraints are investigated to show rigid coupling. Finally, orbital and attitude maneuvers are applied to a singular spacecraft to observe how the joint system is maintained.

II. Problem Statement

The motivation of this work is to fully couple two spacecraft together in 6 DOF. Each of the two spacecraft initially contributes 3 translation and 3 rotation DOF to the overall docked system's DOF. Therefore, there are a total of 12-DOF for the system. It is of interest to remove six of the system's DOF through constraints so that the resulting system has 6-DOF as if it were one singular spacecraft translating and rotating through space. In [4] this was accomplished through two 3-DOF constraints comprised as a single docking arm. This work achieves the same rigid spacecraft coupling using three or more 2-DOF constraints each considered as its own docking arm, where a minimum of three accomplishes the full 6-DOF constraint. The spacecraft system geometry of interest showing these degrees of freedom is illustrated in Fig. 2. In this setup both the $\mathcal{B}_1$ and $\mathcal{B}_2$ frames can translate and rotate to provide the initial 12-DOF.
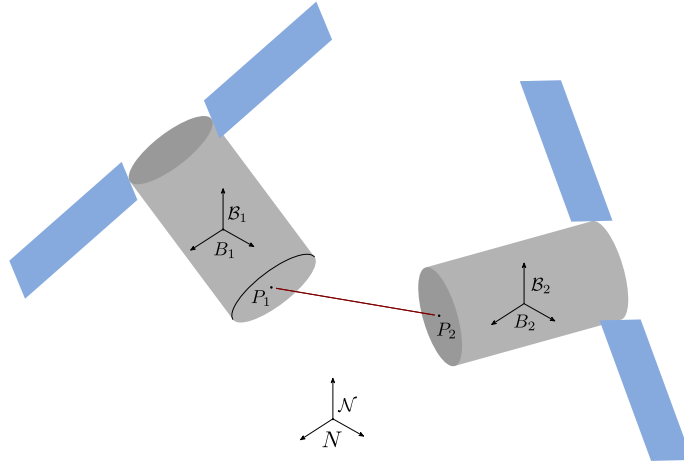
Fig. 2   Spacecraft system geometry, variables, and coordinate frames used for this derivation.

Two types of constraint arms are investigated in this work. The first constraint is a linear sliding arm constraint, where point P_2 on spacecraft two is constrained to move along a line relative to point P_1 on spacecraft one defined in its local $\mathcal{B}_1$ frame. This 2-DOF constraint reduces the degrees of freedom of the system from 12 to 10. A second 2-DOF constraint is implemented where spacecraft two is constrained to follow planar circular motion relative to P_1 on spacecraft one. Finally, combinations of three of the linear sliding arms or rotating arms are used to lock the full 6-DOF between the spacecraft. Fig. 3 illustrates the three constraint formulations considered.

III. Mathematical Overview

A holonomic constraint ψ is a one-dimensional equation that depends on the system's generalized coordinates q_i:

$$\psi(q_1, ..., q_n) = 0 \tag{1}$$

The constraint is enforced through a constraint force that is implemented into the system equations of motion:

$$\boldsymbol{F}_c = \lambda \nabla \psi \tag{2}$$

(a) Sliding arm constraint.

(b) Rotating arm constraint.

(c) Multiple arms achieving a rigid constraint.
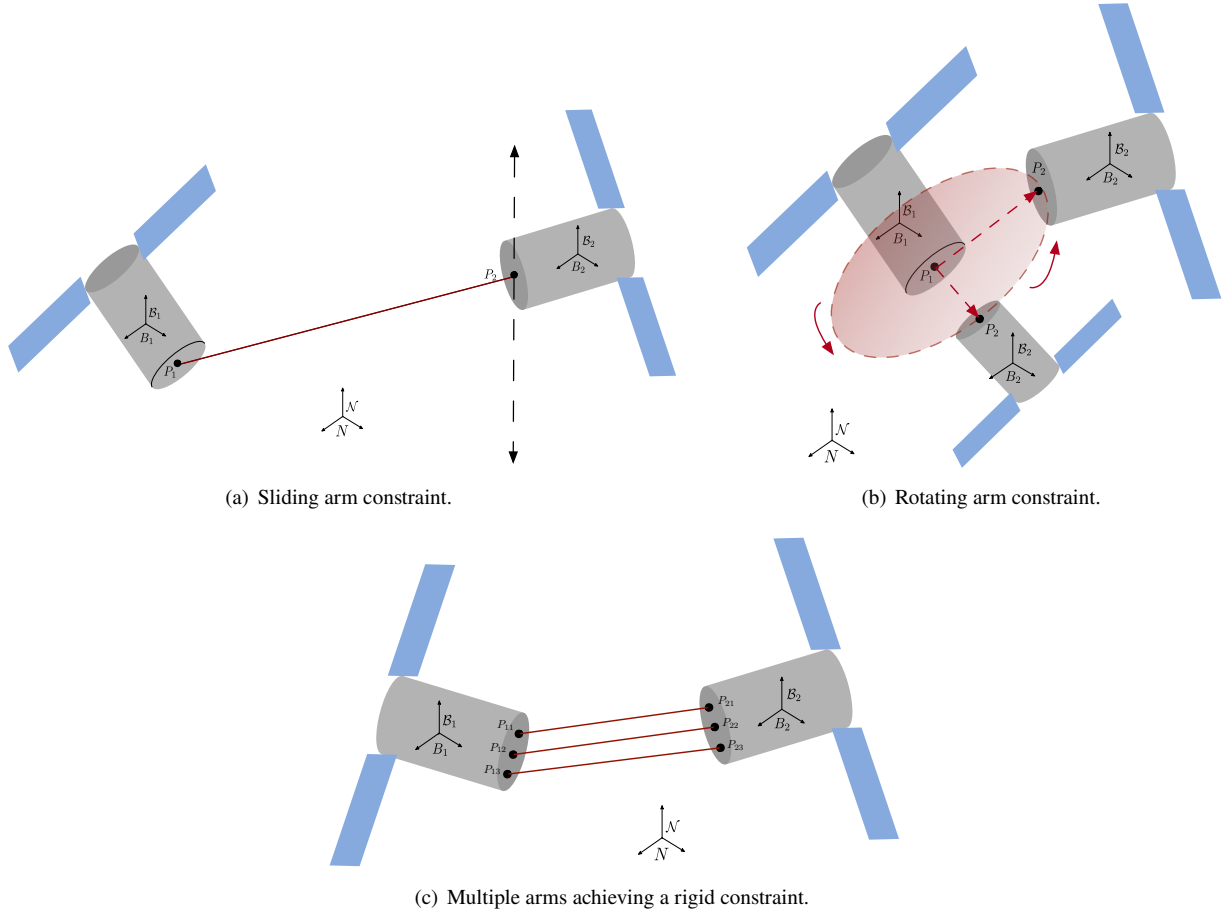
Fig. 3   Implemented constraint types.

where λ is a Lagrange multiplier and ∇ is the spatial derivative operator. The spatial derivative ensures that the constraint force acts perpendicular to the constraint surface. This enforces the system motion to remain on the constraint surface, and hence ensures that the system does not violate the given constraints.

The Lagrange multiplier in a formulation with complex spacecraft can be difficult to solve for analytically. To get around this, the BSM is utilized where a proportional-derivative (PD) controller acts to feed back on the scalar violation of the constraint and constraint rate of change:

$$\lambda = k\psi + c\dot{\psi} \tag{3}$$

Although effective at scaling the constraint force, this method does demand careful balancing of the simulation time-step along with the gain values in order to ensure stability.

A. Constraint Formulations

To formulate the constraint arms, the translational states of connection points P_1 and P_2 are considered in the inertial reference frame $\mathcal{N}$:

$$\mathcal{N}\boldsymbol{r}_{P_1/N} = {}^{\mathcal{N}}\begin{bmatrix} x_{P_1} \\ y_{P_1} \\ z_{P_1} \end{bmatrix}, \qquad \mathcal{N}\boldsymbol{r}_{P_2/N} = {}^{\mathcal{N}}\begin{bmatrix} x_{P_2} \\ y_{P_2} \\ z_{P_2} \end{bmatrix} \tag{4}$$

4

The derivatives of these vectors with respect to the inertial frame are also considered as:

$$
{}^{N}\left(\frac{{}^{N}\mathrm{d}}{\mathrm{d}t}\boldsymbol{r}_{P_1/N}\right) = {}^{N}\dot{\boldsymbol{r}}_{P_1/N} = {}^{N}\begin{bmatrix}\dot{x}_{P_1}\\ \dot{y}_{P_1}\\ \dot{z}_{P_1}\end{bmatrix}, \qquad {}^{N}\left(\frac{{}^{N}\mathrm{d}}{\mathrm{d}t}\boldsymbol{r}_{P_2/N}\right) = {}^{N}\dot{\boldsymbol{r}}_{P_2/N} = {}^{N}\begin{bmatrix}\dot{x}_{P_2}\\ \dot{y}_{P_2}\\ \dot{z}_{P_2}\end{bmatrix} \tag{5}
$$

The position and velocity vectors of point P_2 relative to P_1 can then be written as:

$$
{}^{N}\boldsymbol{r}_{P_2/P_1} = {}^{N}\boldsymbol{r}_{P_2/N} - {}^{N}\boldsymbol{r}_{P_1/N} = {}^{N}\begin{bmatrix}x_{P_2} - x_{P_1}\\ y_{P_2} - y_{P_1}\\ z_{P_2} - z_{P_1}\end{bmatrix}, \qquad {}^{N}\dot{\boldsymbol{r}}_{P_2/P_1} = {}^{N}\dot{\boldsymbol{r}}_{P_2/N} - {}^{N}\dot{\boldsymbol{r}}_{P_1/N} = {}^{N}\begin{bmatrix}\dot{x}_{P_2} - \dot{x}_{P_1}\\ \dot{y}_{P_2} - \dot{y}_{P_1}\\ \dot{z}_{P_2} - \dot{z}_{P_1}\end{bmatrix} \tag{6}
$$

B. Sliding Arm Constraint

The sliding arm constraint restricts spacecraft two to linear motion relative to spacecraft one. This constraint is formulated by fixing the distance of P_2 relative to P_1 along two orthogonal axes of motion i. Modelling a telescoping arm in any arbitrary direction can be performed by specifying i to be two principle axes of an alternative reference frame aligned with the arm and with its origin at the base P_1. For the purposes of validating this constraint the two orthogonal axes of motion are chosen in this paper to be subsets of the three principle axes of the chaser body frame $\mathcal{B}_1$:

$$
\psi^i = \left({}^{\mathcal{B}_1}\boldsymbol{r}_{P_2/P_1}\right)^i - \left({}^{\mathcal{B}_1}\boldsymbol{R}\right)^i \tag{7}
$$

where $i = 2, 3$ for linear motion along the spacecraft one body x-axis, $i = 1, 3$ for motion along the body y-axis, or $i = 1, 2$ for motion along the body z-axis. Note that this defines a line relative to P_1 in the $\mathcal{B}_1$ reference frame as the vector $\boldsymbol{r}_{P_2/P_1}$ is rotated to be evaluated in. The desired connecting arm vector between points P_2 and P_1 is denoted $\boldsymbol{R}$.

The constraint time derivatives are:

$$
\dot{\psi}^i = \left({}^{\mathcal{B}_1}\dot{\boldsymbol{r}}_{P_2/P_1}\right)^i \tag{8}
$$

Taking the spatial gradient of the scalar constraints for $i = 1, 2$ gives the constraint force acting on points P_1 and P_2 where $[\mathcal{N}\mathcal{B}_1]$ is the direction cosine matrix rotation from the body frame $\mathcal{B}_1$ to the inertial frame N:

$$
{}^{N}\boldsymbol{F}_{P_1} = [\mathcal{N}\mathcal{B}_1]\,{}^{\mathcal{B}_1}\begin{bmatrix}-\lambda^1\\ -\lambda^2\\ 0\end{bmatrix}, \qquad {}^{N}\boldsymbol{F}_{P_2} = [\mathcal{N}\mathcal{B}_1]\,{}^{\mathcal{B}_1}\begin{bmatrix}\lambda^1\\ \lambda^2\\ 0\end{bmatrix} \tag{9}
$$

where λ^i is the Lagrange multiplier from constraint ψ^i. Note that the forces are equal and opposite, meaning that when the system is considered as a whole, these forces cancel one another out.

Because the constraint forces are acting on points not coincident with either spacecraft's center of mass (COM), a torque is produced about the COM of each spacecraft:

$$
\boldsymbol{L}_{B_1} = \boldsymbol{r}_{P_1/B_1} \times \boldsymbol{F}_{P_1} \qquad \boldsymbol{L}_{B_2} = \boldsymbol{r}_{P_2/B_2} \times \boldsymbol{F}_{P_2} \tag{10}
$$

C. Rotating Arm Constraint

The rotating arm constraint restricts the motion of connection point P_2 to connection point P_1 to follow a specified azimuth angle ϕ or elevation angle θ considering the arm defined through spherical coordinates with specified fixed scalar arm length R. The azimuth angle is measured counter-clockwise from the positive x-axis, and the elevation angle is measured from the positive z-axis. This 2-DOF constraint imposes that the position vector between points P_2 and P_1 sweeps out a cone shape with its vertex at P_1. Let the position of P_2 be defined in spherical coordinates relative to P_1, noting that $\boldsymbol{r}_{P_2/P_1}$ is now expressed in the body frame $\mathcal{B}_1$:

$$
{}^{\mathcal{B}_1}\boldsymbol{r}_{P_2/P_2} = {}^{\mathcal{B}_1}\begin{bmatrix}x_{P_2/P_1}\\ y_{P_2/P_1}\\ z_{P_2/P_1}\end{bmatrix} = {}^{\mathcal{B}_1}\begin{bmatrix}R\sin(\theta)\cos(\phi)\\ R\sin(\theta)\sin(\phi)\\ R\cos(\theta)\end{bmatrix} \tag{11}
$$

Therefore the constraints can be defined as utilizing a length constraint ψ_r shown in Eq. (12) plus a second constraint either fixing the azimuth angle as shown in Eq. (13) or the elevation angle as shown in Eq. (14).

$$\psi_r = \sqrt{x_{P_2/P_1}^2 + y_{P_2/P_1}^2 + z_{P_2/P_1}^2} - R \tag{12}$$

$$\psi_{az} = \tan^{-1}\left(\frac{y_{P_2/P_1}}{x_{P_2/P_1}}\right) - \phi \tag{13}$$

$$\psi_{el} = \cos^{-1}\left(\frac{z_{P_2/P_1}}{\sqrt{x_{P_2/P_1}^2 + y_{P_2/P_1}^2 + z_{P_2/P_1}^2}}\right) - \theta \tag{14}$$

With the constraints defined, next the time derivative of the constraints must be found in order to use the BSM to define the Lagrange multiplier. Taking the time derivative of the constraints gives Eq. (15) for the length constraint, and Eqs. (16) and (17) for the azimuth and elevation constraint options respectively.

$$\dot{\psi}_r = \frac{\mathbf{r}_{P_2/P_2} \cdot \dot{\mathbf{r}}_{P_2/P_2}}{|\mathbf{r}_{P_2/P_2}|} \tag{15}$$

$$\dot{\psi}_{az} = \frac{x_{P_2/P_1}\dot{y}_{P_2/P_1} - y_{P_2/P_1}\dot{x}_{P_2/P_1}}{x_{P_2/P_1}^2 + y_{P_2/P_1}^2} \tag{16}$$

$$\dot{\psi}_{el} = \frac{z_{P_2/P_1}(x_{P_2/P_1}\dot{x}_{P_2/P_1} + y_{P_2/P_1}\dot{y}_{P_2/P_1}) - \dot{z}_{P_2/P_1}(x_{P_2/P_1}^2 + y_{P_2/P_1}^2)}{(x_{P_2/P_1}^2 + y_{P_2/P_1}^2 + z_{P_2/P_1}^2)\sqrt{x_{P_2/P_1}^2 + y_{P_2/P_1}^2}} \tag{17}$$

Next, the constraint forces acting on each spacecraft must be defined. The constraint force acting on spacecraft one is:

$$\mathbf{F}_{P_1} = \lambda_r \nabla\psi_r + \lambda_2 \nabla\psi_2 \tag{18}$$

where ψ_2 is either ψ_{az} or ψ_{el} with spacial gradients defined as:

$$\nabla\psi_r = \frac{-1}{|\mathbf{r}_{P_2/P_2}|}\begin{bmatrix} x_{P_2/P_1} \\ y_{P_2/P_1} \\ z_{P_2/P_1} \end{bmatrix} \tag{19}$$

$$\nabla\psi_{az} = \frac{-1}{x_{P_2/P_1}^2 + y_{P_2/P_1}^2}\begin{bmatrix} y_{P_2/P_1} \\ x_{P_2/P_1} \\ 0 \end{bmatrix} \tag{20}$$

$$\nabla\psi_{el} = \frac{-1}{(x_{P_2/P_1}^2 + y_{P_2/P_1}^2 + z_{P_2/P_1}^2)\sqrt{x_{P_2/P_1}^2 + y_{P_2/P_1}^2}}\begin{bmatrix} x_{P_2/P_1}z_{P_2/P_1} \\ y_{P_2/P_1}z_{P_2/P_1} \\ -(x_{P_2/P_1}^2 + y_{P_2/P_1}^2) \end{bmatrix} \tag{21}$$

The constraint force acting on P_2 is equal and opposite to the force acting on P_1:

$$\mathbf{F}_{P_2} = -\mathbf{F}_{P_1} \tag{22}$$

and the torque about the COM of each spacecraft is the same as for the linear sliding arm constraint in Eq. (10).

D. Rigid Constraint

The rigid constraint combines three of either arm to lock the full translational and rotational motion of the second spacecraft relative to the first spacecraft by connecting the three arms at different P_1 and P_2 connection points on each spacecraft. It is required that the released axes of all arms not be the same axis. For example, three 2-DOF linear sliding arm constraints can be used to achieve the desired six degree-of-freedom lock as:

$$\psi^1 = \mathbf{r}_{P_{21}/P_{11}}^i - \mathbf{R}_1^i \quad i = 1, 2 \tag{23}$$

6

$$\psi^2 = \boldsymbol{r}^j_{P_{22}/P_{12}} - \boldsymbol{R}^j_2 \quad j = 2, 3 \tag{24}$$

$$\psi^3 = \boldsymbol{r}^k_{P_{23}/P_{13}} - \boldsymbol{R}^k_3 \quad k = 1, 3 \tag{25}$$

Because ψ_1, ψ_2, and ψ_3 each restrict the spacecraft motion along a different axis, the combination of the three constraints locks the full translational and rotational states of spacecraft two relative to spacecraft one. This can similarly be done with three rotating arm constraints.

IV. Numerical Results

The numerical simulation of the different constraints is performed in Matlab. The two spacecraft are placed in a low Earth orbit (LEO), and the mass of the chaser spacecraft (spacecraft one) is approximately half of the mass of the target spacecraft (spacecraft two). The two spacecraft are initialized with the arm extending through the along-track direction of their mutual orbit. Additionally, both spacecraft start with a zero angular rate relative to the inertial frame. The exact simulation parameters are included in Table 1. The results for each simulation run are presented in this section as relative motion plots and constraint violation time history. Note that the relative motion plots are displayed in the $\mathcal{B}_1$ reference frame, and thus only the motion of spacecraft two is shown relative to spacecraft one. Therefore, all plots show points B_1 and P_1 as fixed because they are rigidly attached to spacecraft one. The time history of points B_2 and P_2 are plotted to show the motion of spacecraft two. Grey lines are also plotted to show the connection sequence from B_1 to B_2. The constraint violation plots show the constraint differences calculated by either Eqs. (7) or (12)-(14) at each timestep.

A. Sliding Arm Constraint

First a singular sliding arm is simulated to verify the expected motion. As shown in Fig. 4, the relative x and z directions are constrained and the y direction is released. As expected, this choice results in the motion of P_2 exclusively along the relative y axis. Point B_2 can be seen to trail freely around point P_2. The constraint violations seen in subplot 4(b) also give confidence that the arm is performing as expected. The constraints in the x and z directions stay below 10^{-7} orders of magnitude while the y-axis difference between its initial and current value can be seen to grow unbounded in magnitude. These constraint orders of magnitude are much smaller than the one meter connection arms between hubs B_1 and B_2 to their connection points P_1 and P_2 as well as the one tenth of a meter arm length between P_1 and P_2.

(a) B_1 Relative motion in the $\mathcal{B}_1$ frame.

(b) Linear sliding arm constraint violations per axis.
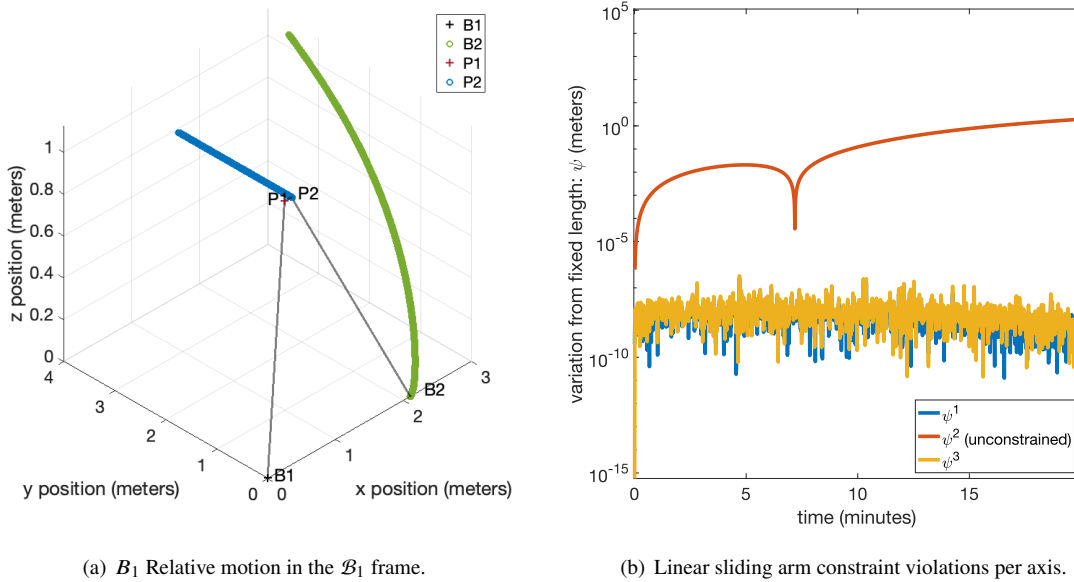
Fig. 4   Singular linear sliding arm constraint performance.

Table 1 Simulation parameters for the joint spacecraft simulation.

Parameter	Notation	Value	Units
Spacecraft 1's mass	m_1	330	kg
Spacecraft 2's mass	m_2	750	kg
Spacecraft 1's inertia about its center of mass	$^{\mathcal{B}_1}[I_{\mathrm{SC}_1,B_1}]$	$\begin{bmatrix} 82 & 0 & 0 \\ 0 & 98 & 0 \\ 0 & 0 & 121 \end{bmatrix}$	kg· m^2
Spacecraft 2's inertia about its center of mass	$^{\mathcal{B}_2}[I_{\mathrm{SC}_2,B_2}]$	$\begin{bmatrix} 900 & 0 & 0 \\ 0 & 800 & 0 \\ 0 & 0 & 600 \end{bmatrix}$	kg· m^2
Spacecraft 1's connection locations P_1 with respect to B_1	$\begin{Bmatrix} ^{\mathcal{B}_1}\boldsymbol{r}_{P_{1,1}/B_1} \\ ^{\mathcal{B}_1}\boldsymbol{r}_{P_{1,2}/B_1} \\ ^{\mathcal{B}_1}\boldsymbol{r}_{P_{1,3}/B_1} \end{Bmatrix}$	$\begin{Bmatrix} ^{\mathcal{B}_1}[1,1,1]^T \\ ^{\mathcal{B}_1}[1,-1,-1]^T \\ ^{\mathcal{B}_1}[1,-1,1]^T \end{Bmatrix}$	m
Spacecraft 2's connection locations P_2 with respect to B_2	$\begin{Bmatrix} ^{\mathcal{B}_2}\boldsymbol{r}_{P_{2,1}/B_2} \\ ^{\mathcal{B}_2}\boldsymbol{r}_{P_{2,2}/B_2} \\ ^{\mathcal{B}_2}\boldsymbol{r}_{P_{2,3}/B_2} \end{Bmatrix}$	$\begin{Bmatrix} ^{\mathcal{B}_2}[-1,1,1]^T \\ ^{\mathcal{B}_2}[-1,-1,-1]^T \\ ^{\mathcal{B}_2}[-1,-1,1]^T \end{Bmatrix}$	m
Spacecraft 2's connection locations P_2 with respect to P_1	$\begin{Bmatrix} ^{\mathcal{B}_1}\boldsymbol{R}_{P_{2,1}/P_{1,1}} \\ ^{\mathcal{B}_1}\boldsymbol{R}_{P_{2,2}/P_{1,2}} \\ ^{\mathcal{B}_1}\boldsymbol{R}_{P_{2,3}/P_{1,3}} \end{Bmatrix}$	$\begin{Bmatrix} ^{\mathcal{B}_1}[0.1,0,0]^T \\ ^{\mathcal{B}_1}[0.1,0,0]^T \\ ^{\mathcal{B}_1}[0.1,0,0]^T \end{Bmatrix}$	m
DCM of the initial B_1 frame with respect to the inertial N frame	$[\mathcal{B}_1\mathcal{N}]$	$\begin{bmatrix} 1 & 0 & 0 \\ 0 & 1 & 0 \\ 0 & 0 & 1 \end{bmatrix}$	–
DCM of the initial B_2 frame with respect to the inertial N frame	$[\mathcal{B}_2\mathcal{N}]$	$\begin{bmatrix} 1 & 0 & 0 \\ 0 & 1 & 0 \\ 0 & 0 & 1 \end{bmatrix}$	–
Spacecraft 1's initial angular velocity	$^{\mathcal{B}_1}\boldsymbol{\omega}_{B_1/N}$	$^{\mathcal{B}_1}[0,0,0]^T$	rad/sec
Spacecraft 2's initial angular velocity	$^{\mathcal{B}_2}\boldsymbol{\omega}_{B_2/N}$	$^{\mathcal{B}_2}[0,0,0]^T$	rad/sec
Baumgarte Stabilization proportional gain	k	1E6	–
Baumgarte Stabilization derivative gain	c	2E3	–
Orbital maneuver thrust vector	$^{\mathcal{B}_1}\boldsymbol{F}$	$^{\mathcal{B}_1}[-0.25,0,0]^T$	N
Attitude maneuver proportional feedback gain	p	60	–
Attitude maneuver derivative feedback gain	d	40	–

B. Rotating Arm Constraint

Next, an individual rotating arm is simulated to verify the constraint development. The goal is to create an arm that follows circular motion about P_1 with P_1 in the plane, but not all specified elevation angles achieve this. Elevation angles other than 90° result in motion of the arm between P_2 and P_1 sweeping out a cone with its tip at P_1 and its body pointed through the z-axis. This result initially motivated use of the azimuth constraint, where a specified azimuth angle and free elevation angle causes P_2 to follow the desired circular motion. However, once the elevation angle neared 0° or 180°, both the x and y coordinates shrink to zero, exposing a singularity in Eq. (13), for which the constraint is undefined. To circumvent this problem, a fixed elevation angle of 90° is selected utilizing Eqs. (12) and (14), while Eq. (13) is left free.

The simulation results for the single rotating arm are shown in Fig. 5. The resulting relative motion verifies the developed constraint, as P_2 can be seen to rotate about P_1 in the xz-plane with the COM B_2 trailing freely behind. The constraint violations also confirm the expected behavior, as both ϕ_r and ϕ_{el} stay bounded below 10^{-4} order of magnitude meters and radians respectively while the azimuth angle accordingly grows unbounded.

(a) B_1 Relative motion in the $\mathcal{B}_1$ frame.

(b) Rotating arm constraint violations.
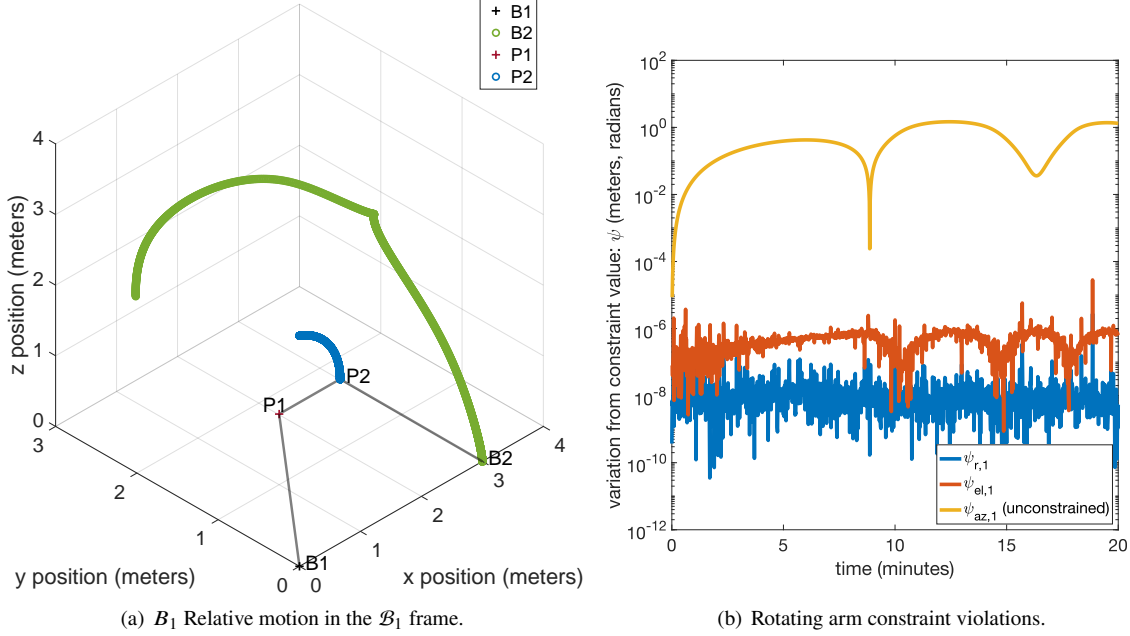
Fig. 5   Singular rotating arm constraint performance.

C. Rigid Constraint

With the verification of the individual 2-DOF constraint arms, the next step is to combine multiple arms to achieve a rigid 6-DOF coupling between the spacecraft. Sets of three arms are implemented and the results are included below. As discussed in the problem statement, a goal of this work is to develop a rigid 6-DOF constraint utilizing multiple arms. Because each individual arm constrains 2-DOF, implementing three arms will create a 6-DOF constraint if the free DOF selected is different for each arm. The 6-DOF coupling in the context of the relative motion plot should illustrate points P_2 and B_2 remaining stationary. In the context of the constraint violation plots, it is expected for all constraints to be satisfied despite one axis of each arm being free. The existence of three arms ensures that all constraints are inherently maintained.

This hypothesis is first tested with the sliding arm as shown in Fig. 6. As expected, each of the connection points P_2 remain stationary in the $\mathcal{B}_1$ frame as well as point B_2. The constraint violation plot also confirms the expected behavior showing all three arms peaking around 10^{-8} meters. Note that these constraint violations in Fig. 6(b) display the 2-norm of all three axes are for each arm instead of individual axes constraint violations as was shown in Fig. 4(b).

In order to have mutually exclusive axes between the different rotating arms while still using the elevation constraint, the x, y, and z coordinates were swapped in Eq. (14) to change what principal axis the elevation angle is defined about. It was ensured that the coordinates were swapped such that a right-handed coordinate system is maintained. Doing so resulted in the simulation performance shown in Fig. 7. Once again, all connection points P_2 as well as point B_2 remain fixed in the $\mathcal{B}_1$ frame. Both the relative motion and constraint violations confirm that this multi-arm formulation with rotating arms appropriately couples the two spacecraft in 6-DOF. All constraint violations remain below 10^{-5} meters and radians, consistently smaller than with a single rotating arm thanks to the slower joint spacecraft motion when fully coupled.

D. Perturbation Analysis

Although the rigid constraint analysis shows that this method is effective at yielding adequately small constraint violations, it has only considered the slow motion of free-floating spacecraft. Performance is further assessed by applying perturbations that stress the constraints. For this analysis, both rigid implementations of three sliding arms and three rotating arms are tested. Each maneuver only applies forces or torques to the chaser spacecraft, assuming a scenario in which the target spacecraft does not contribute control and the arm between them is therefore stressed greater than if the target spacecraft was cooperative. The first maneuver tested is an orbital maneuver adding a small but sustained translational perturbation by applying a force representative of low-thrust electric propulsion. The perturbation

(a) B_1 Relative motion in the $\mathcal{B}_1$ frame.

(b) Linear sliding arm constraint violation magnitudes for each arm.
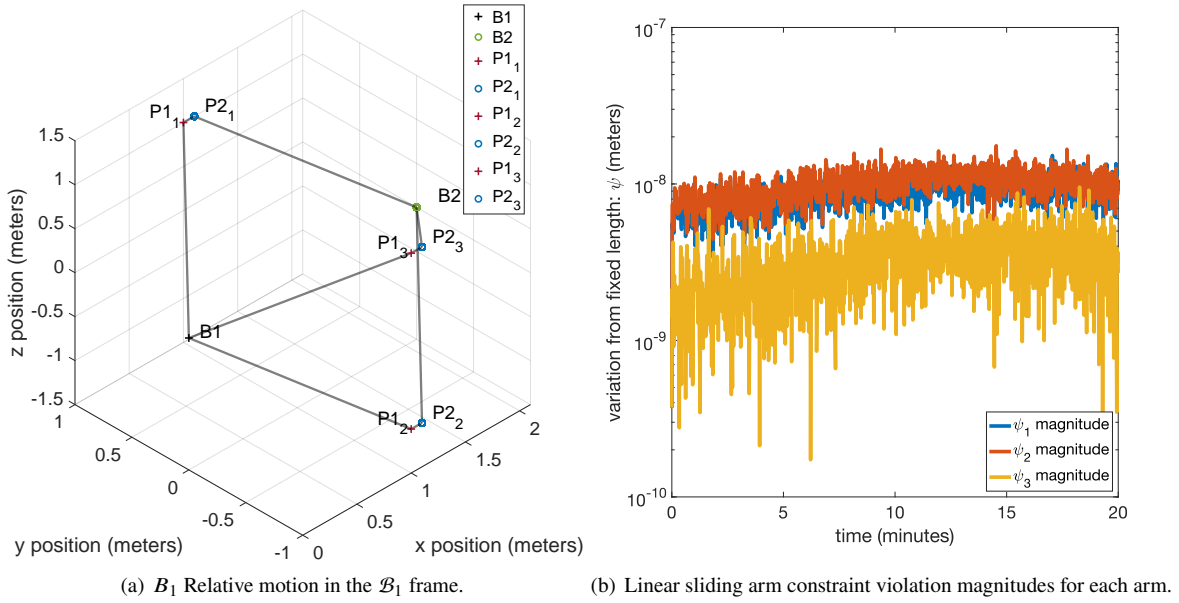
Fig. 6   Three linear sliding arm constraints performance.

(a) B_1 Relative motion in the $\mathcal{B}_1$ frame.

(b) Rotating arm constraint violations for each arm.
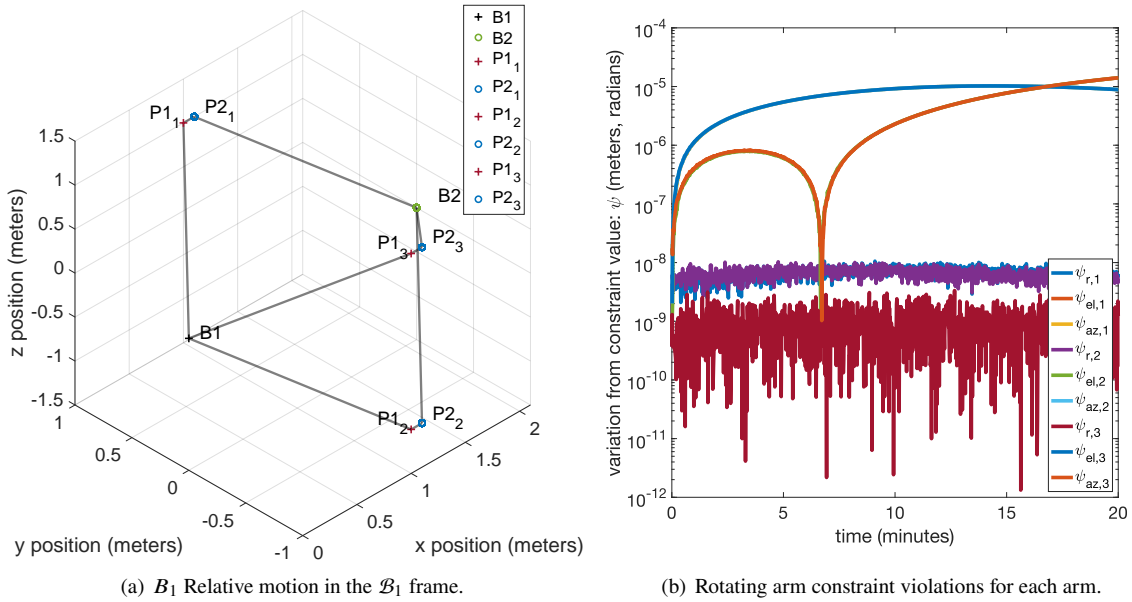
Fig. 7   Three rotating arm constraints performance.

is turned on at minute five and lasts two minutes. The resulting performance of the rigid constraint using the sliding arms is shown in Fig. 8(a) and rotating arms are shown in Fig. 8(b).

Prior to initiation of the orbital maneuver at minute five, the constraint violations for both formulations remain at nominally small orders of magnitude similar to the unperturbed scenarios in Figures 6(b) and 7(b). While the translational force is applied to spacecraft one between minutes five and seven, the constraint violations increase as a new equilibrium is reached due to spacecraft one's excited motion. The oscillatory pattern of the constraint violations at this stage is due to the log scale plotting as the constraint bounces back and forth across zero. This is simply a macro
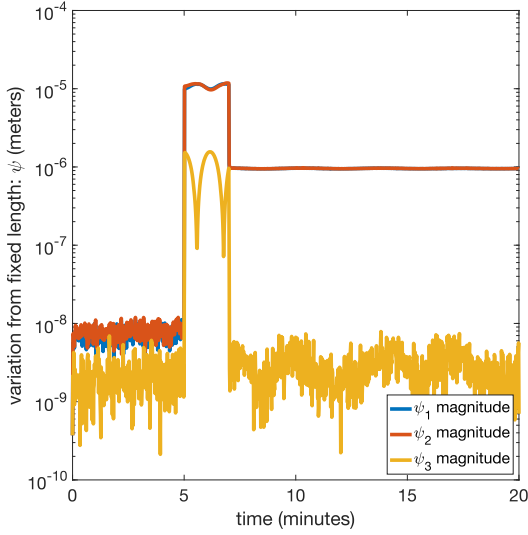
(a) Linear sliding arm constraint violations for each arm.
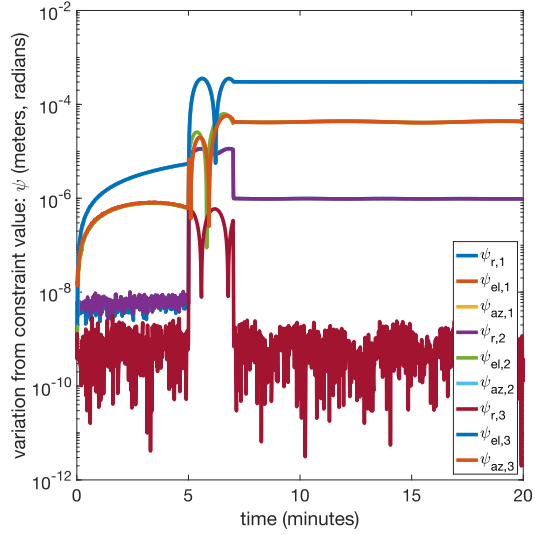
(b) Rotating arm constraint violations for each arm.

Fig. 8   Three arm rigid constraint performance with orbital maneuver applied.

version of the otherwise seeming noise at smaller orders of magnitude before the force is applied. After the maneuver force is turned off at minute seven, some of the constraint violations drop back down to their pre-maneuver order of magnitude while others settle at a new equilibrium. The higher new equilibria are due to a spin imparted on the joint spacecraft system by the translational force not being perfectly aligned with the combined center of mass of the two spacecraft. The spin rate demands a centripetal force from the connecting arm on each spacecraft and the constraint violations vary more with this dynamic motion. Despite the increase, the constraint violations both during and after the maneuver remain at least several orders of magnitude smaller than the size of the respective spacecraft.

Next an attitude maneuver is tested, applying a torque to the chaser spacecraft starting at minute five until it rotates it by 22.5°. The MRP feedback attitude control law used is shown in Eq. (26) where $\sigma_{B_1/R}$ is the attitude error between the $\mathcal{B}_1$ frame and a reference frame $\mathcal{R}$ initially 22.5° offset about the $\mathcal{B}_1$ z-axis.

$$^{\mathcal{B}_1}\boldsymbol{L}_{\text{ext}} = p\boldsymbol{\sigma}_{B_1/R} + d\,^{\mathcal{B}_1}\boldsymbol{\omega}_{B_1/R} \tag{26}$$

The resulting performance for the sliding arm and rotating arm constraints are shown in Figures 9(a) and 9(b) respectively. Once again the constraint violations can be seen to increase at the start of the maneuver as spacecraft one begins its rotation and the constraint arm enforces commensurate motion by spacecraft two. Due to the nature of this attitude maneuver asymptotically closing in to its desired rotation, the eventual setting of the spacecraft motion results in a far calmer post-maneuver state compared to the translational maneuver. When the maneuver reaches its desired attitude around minute ten, the new equilibrium constraint violations are only slightly higher than they were pre-maneuver.

(a) Linear sliding arm constraint violations for each arm.

(b) Rotating arm constraint violations for each arm.
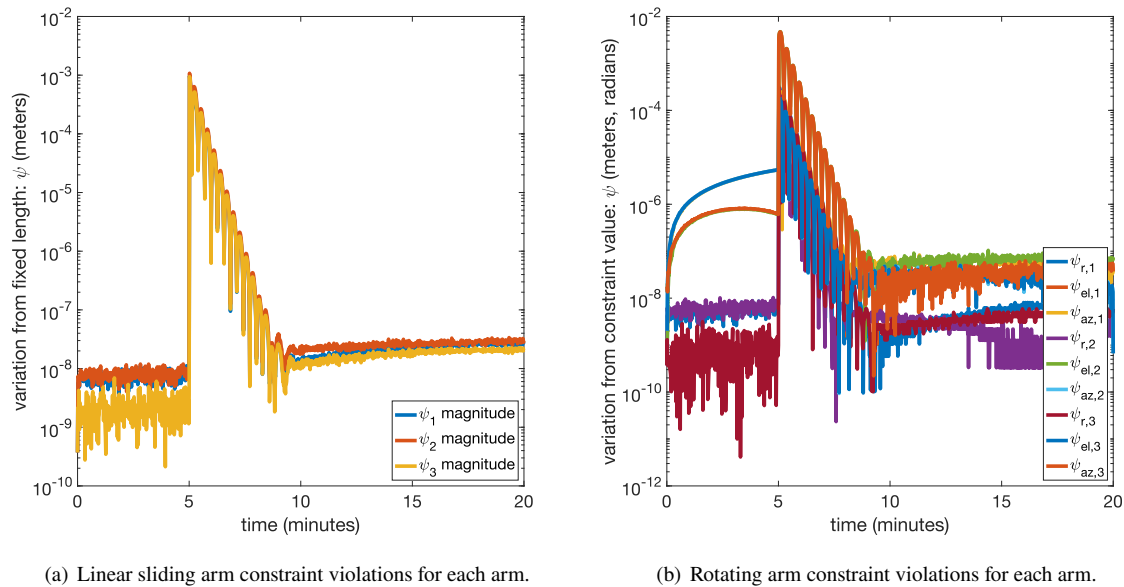
Fig. 9   Three arm rigid constraint performance with attitude maneuver applied.

V. Conclusions

Whereas prior work investigated several types of single-arm holonomic constraints, this paper derives and implements multiple simultaneous constraints to simulate multi-arm coupling between two spacecraft. First, constraint formulations for both an individual sliding arm and rotating arm were developed such that they constrained 2-DOF and a system of combining multiple arms was laid out. Next the individual arm constraints were implemented in software to confirm that the resulting spacecraft motion satisfied the constraint formulation by releasing desired DOF. Finally, two rigid constraints were implemented in software as a combination of either three sliding arm or three rotating arm constraints. Both rigid constraints demonstrated the expected behavior of full 6-DOF coupling between the two spacecraft with constraint violations many orders of magnitude smaller than the size of each individual spacecraft and their connecting arm. When applying orbital and attitude maneuvers to the chaser spacecraft, the constraints maintained coupled motion with small constraint violations relative to vehicle size, showing that this method of simulation joint spacecraft systems can handle more realistic dynamic scenarios. As the demand for satellite servicing increases, such post-docked dynamical simulation will be increasingly required as well. Rapid dynamics simulation is valuable at the servicer design phase evaluating vehicle choices when docked to different clients, at the client selection phase when evaluating whether a potential client vehicle can be serviced, and at the inspection phase of a mission when updated information about the client vehicle needs to be implemented to re-evaluate preliminary dynamical simulation. Using techniques such as this constrained dynamics methodology contributes to an efficient simulation by eliminating the need for a surrogate single spacecraft model to be simultaneously maintained.

References

[1] Benedict, B. L., "Rationale for need of in-orbit servicing capabilities for GEO spacecraft," *AIAA SPACE 2013 Conference and Exposition*, 2013, p. 5444.

[2] Corbin, B. A., Abdurrezak, A., Newell, L. P., Roesler, G. M., and Lal, B., "Global Trends in On Orbit Servicing, Assembly and Manufacturing (OSAM)," 2020. https://doi.org/10.2514/6.2013-5444.

[3] Baumgarte, J., "Stabilization of constraints and integrals of motion in dynamical systems," *Computer Methods in Applied Mechanics and Engineering*, Vol. 1, No. 1, 1972, pp. 1–16. https://doi.org/https://doi.org/10.1016/0045-7825(72)90018-7, URL https://www.sciencedirect.com/science/article/pii/0045782572900187.

[4] Carneiro, J. V., Morell, A., and Schaub, H., "Post-Docking Spacecraft Dynamics Using Baumgarte Stabilization," *AAS Spaceflight Mechanics Meeting*, Austin, TX, 2023. Paper No. AAS 23–148.

[5] Carneiro, J. V., Morell, A., and Schaub, H., "Post-Docking Complex Spacecraft Dynamics Using Baumgarte Stabilization," *AAS Astrodynamics Specialist Conference*, Big Sky, MT, 2023. Paper No. AAS 23-148.

[6] Kenneally, P. W., Piggott, S., and Schaub, H., "Basilisk: A Flexible, Scalable and Modular Astrodynamics Simulation Framework," *Journal of Aerospace Information Systems*, Vol. 17, No. 9, 2020, pp. 496–507.

[7] Alcorn, J., Allard, C., and Schaub, H., "Fully Coupled Reaction Wheel Static and Dynamic Imbalance for Spacecraft Jitter Modeling," *AIAA Journal of Guidance, Control, and Dynamics*, Vol. 41, No. 6, 2018, pp. 1380–1388. https://doi.org/10.2514/1.G003277.

[8] Allard, C., Schaub, H., and Piggott, S., "General Hinged Solar Panel Dynamics Approximating First-Order Spacecraft Flexing," *AIAA Journal of Spacecraft and Rockets*, Vol. 55, No. 5, 2018, pp. 1290–1298. https://doi.org/10.2514/1.A34125.

[9] Panicucci, P., Allard, C., and Schaub, H., "Volume Multi-Sphere-Model Development Using Electric Field Matching," *Journal of Astronautical Sciences*, Vol. 65, No. 4, 2018, pp. 423–447. https://doi.org/10.1007/s40295-018-0133-0.

[10] Redd, N. T., "Bringing satellites back from THE DEAD: Mission extension vehicles give defunct spacecraft a new lease on life," *IEEE Spectrum*, Vol. 57, 2020, pp. 6–7.

[11] Shoemaker, M. A., Vavrina, M., Gaylor, D. E., Mcintosh, R., Volle, M., and Jacobsohn, J., "OSAM-1 decommissioning orbit design," *AAS/AIAA Astrodynamics Specialis t Conference*, 2020.

[12] Biesbroek, R., Aziz, S., Wolahan, A., Cipolla, S.-f., Richard-Noca, M., and Piguet, L., "The clearspace-1 mission: Esa and clearspace team up to remove debris," *Proc. 8th Eur. Conf. Sp. Debris*, 2021, pp. 1–3.

[13] Harris, T., Brettle, H., Lecas, M., Blacketer, L., Carr, A., Fernandez, A., and Puppa, A., "An exploration of opportunities to advance ground-based and space-based SSA systems through in-orbit demonstration missions," 2021.

[14] Gasbarri, P., and Pisculli, A., "Dynamic/control interactions between flexible orbiting space-robot during grasping, docking and post-docking manoeuvres," *Acta Astronautica*, Vol. 110, 2015, pp. 225–238. https://doi.org/https://doi.org/10.1016/j.actaastro.2015.01.024, URL https://www.sciencedirect.com/science/article/pii/S0094576515000399, dynamics and Control of Space Systems.

[15] Stolfi, A., Gasbarri, P., and Misra, A. K., "A two-arm flexible space manipulator system for post-grasping manipulation operations of a passive target object," *Acta Astronautica*, Vol. 175, 2020, pp. 66–78. https://doi.org/https://doi.org/10.1016/j.actaastro.2020.04.045, URL https://www.sciencedirect.com/science/article/pii/S0094576520302605.